NANO LETTERS

pubs.acs.org/NanoLett Letter

Fast-Response Flexible Temperature Sensors with Atomically Thin Molybdenum Disulfide

Alwin Daus, Marc Jaikissoon, Asir Intisar Khan, Aravindh Kumar, Ryan W. Grady, Krishna C. Saraswat, and Eric Pop*

Cite This: *Nano Lett.* 2022, 22, 6135−6140 Read Online

ACCESS | Metrics & More | Article Recommendations | Supporting Information

ABSTRACT: Real-time thermal sensing on flexible substrates could enable a plethora of new applications. However, achieving fast, sub-millisecond response times even in a single sensor is difficult, due to the thermal mass of the sensor and encapsulation. Here, we fabricate flexible monolayer molybdenum disulfide (MoS_2) temperature sensors and arrays, which can detect temperature changes within a few microseconds, over 100× faster than flexible thin-film metal sensors. Thermal simulations indicate the sensors' response time is only limited by the MoS_2 interfaces and encapsulation. The sensors also have high temperature coefficient of resistance, ∼1−2%/K and stable operation upon cycling and long-term measurement when they are encapsulated with alumina. These results, together with their biocompatibility, make these devices excellent candidates for biomedical sensor arrays and many other Internet of Things applications.

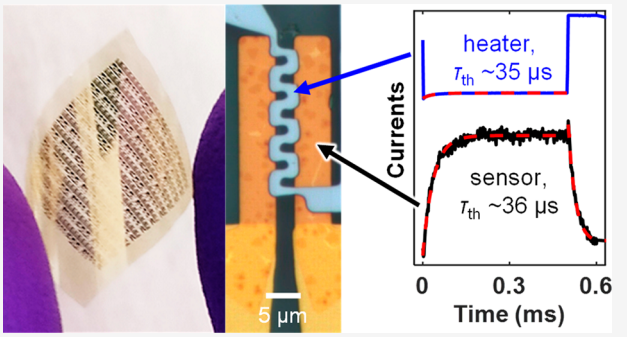

KEYWORDS: *two-dimensional materials, monolayer, molybdenum disulfide, flexible sensors, temperature, real-time*

Fast and accurate thermal measurements are needed in biomedical applications,[1,2] wearables,[3] robotics,[4] environmental monitoring,[5] and safety-critical machine management.[6] Hence, realizing temperature sensors on ultrathin, conformal, and flexible substrates is important to allow for improved interfacing with biological tissue such as skin,[1] and it simplifies the integration in disposable packaging (e.g., for food monitoring)[5,7] or tight spaces in machines or electronic components (e.g., power electronics).[8] Furthermore, some applications require high spatial resolution and mapping of temperature in real time:[9] for example, arrays of micrometer-scale temperature sensors could be used on electronic skin,[10] to detect skin[11] or breast[12] cancer at an early stage or to observe local infections that can occur during wound healing (e.g., after surgery).[13,14]

Recently, low-dimensional materials such as graphene and carbon nanotubes have become popular candidates for flexible temperature sensors with good sensitivity.[15] However, emerging two-dimensional (2D) semiconductors such as molybdenum disulfide (MoS_2) have been largely unexplored for such applications. Prior works on MoS_2 have indicated promise due to its biocompatibility[16] and high temperature coefficient of resistance (TCR),[17] but its real-time sensing performance and potential for array integration remain unknown.

In this work, we demonstrate flexible monolayer MoS_2 temperature sensors on thin (∼5 μm) flexible substrates fabricated by a recently developed direct transfer technique.[18] The sensors exhibit high TCRs of ∼1−2%/K between 27 and 120 °C and a stable response after a thin (∼35 nm) alumina encapsulation. Furthermore, we determine a thermal time constant of <36 μs (limited by our integrated Ti/Pd microheaters), which is >100× faster than previously shown flexible thin-film metal sensors.[1] We also realize 4 × 4 arrays of our MoS_2 temperature sensors to demonstrate the feasibility of this material and integration approach for temperature mapping.

Figure 1a summarizes the device fabrication process. First, continuous monolayer MoS_2 films are grown on SiO_2/Si by chemical vapor deposition (details are given in refs 19 and 20). Before the films are transferred to flexible substrates, Au metal contacts are deposited and the MoS_2 film is patterned. Then, a ∼5 μm thick flexible polyimide (PI) substrate is spin-coated on top. This ensures a very smooth MoS_2 interface with the PI, with a surface roughness of ∼0.4 nm (Supplementary Section 2 in ref 18). MoS_2 and Au both have low adhesion to SiO_2, which enables a simple release in deionized (DI) water while

Received: April 3, 2022
Revised: July 3, 2022
Published: July 28, 2022

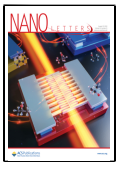

https://doi.org/10.1021/acs.nanolett.2c01344
Nano Lett. 2022, 22, 6135−6140

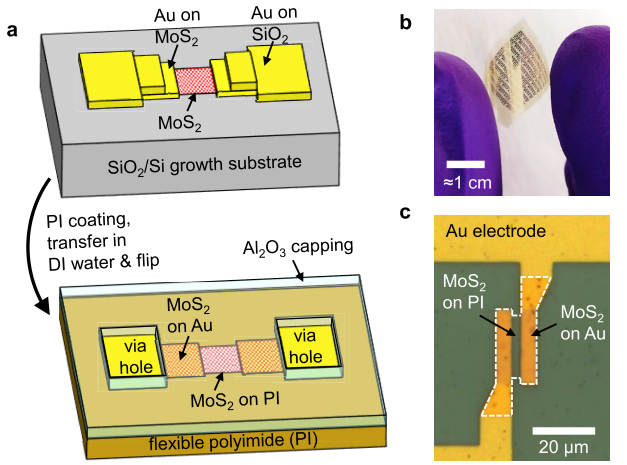

Figure 1. Flexible monolayer MoS_2 temperature sensors. (a) Schematic of the fabrication process and sensor structure. Optical images of (b) the flexible substrate with sensor arrays and (c) a single resistive sensor, encapsulated with alumina. The dashed line marks the outline of the MoS_2, and the different colors can be attributed to different thicknesses of Au below MoS_2.

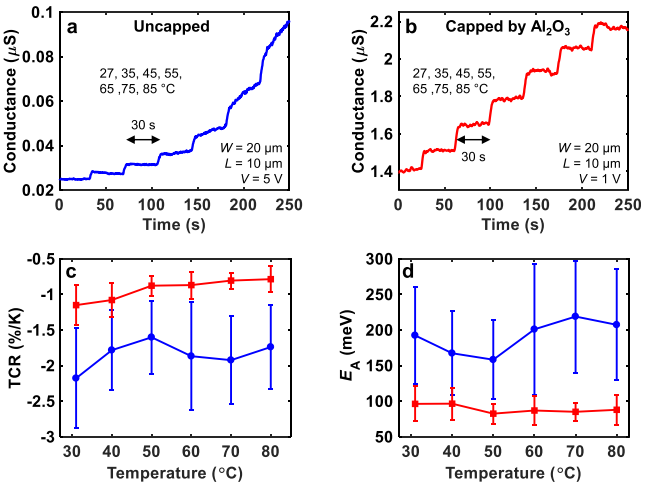

Figure 2. Real-time sensing performance before and after sensor encapsulation with ~35 nm of Al_2O_3. Conductance vs time for (a) an uncapped and (b) a capped sensor with a width W = 20 μm and a length L = 10 μm biased at voltages V = 5 and 1 V, respectively. There are seven temperature steps, at 27 and 35 °C and then in 10 °C increments up to 85 °C. The temperature steps are ramped at 150 °C/min, and then the temperature is held for 30 s at each point. (c) Extracted differential temperature coefficient of resistance (TCR) and (d) activation energy E_A averaged over five sensors. Error bars denote the standard deviations. Legend: blue circles, uncapped; red squares, capped.

they are supported by the flexible PI.[18] Finally, devices are encapsulated with ~35 nm thick Al_2O_3 and holes for probing are formed. The monolayer MoS_2 has good crystallinity with a grain size of tens of micrometers, and the quality is preserved throughout the fabrication process.[18−20] (Transistors fabricated on the same substrate as our sensors display good mobility up to ~20 $cm^2\ V^{-1}\ s^{-1}$, as shown in Figure S1.) In Section S4 in the Supporting Information, we briefly discuss how different MoS_2 qualities may affect sensor behavior, and additional details of our fabrication and release process can be found in refs 18 and 21. Figure 1b,c displays optical images of the flexible PI substrate and a temperature sensor after fabrication, respectively. The mechanical flexibility of similar device stacks (but with MoS_2 transistors) was evaluated in detail in ref 18, where it was found that the thin PI substrate enables bendability to a radius of 4 mm and below.

During our initial electrical characterization, we found that the microscope light, used for probing the contact pads, led to some charge generation and trapping that persists even after the light was turned off. This caused a baseline drift of our sensors, which vanished after repeated measurements (see Figure S2) or after annealing at 120 °C for 15−20 min. Thus, we performed all subsequent measurements in the dark, in air after an initial annealing as specified above. We used two-point measurements for the sensors, and their electrical characteristics are dominated by the MoS_2 channel properties rather than any contact effects due to micrometer-scale channel lengths and a comparatively low contact resistance (R_C) with Au contacts (see Figure S4).[18,22]

Figure 2 presents a comparison of the sensor responses before and after the Al_2O_3 encapsulation. We applied a staircase-like temperature sweep from 27 to 85 °C with 30 s hold time at each temperature. It is apparent that the conductance in uncapped sensors (Figure 2a) is still increasing even after the temperature has already settled at its operating point, while it is stable for the sensors capped with Al_2O_3 (Figure 2b).

The continued increase in conductance of uncapped devices after heating can be attributed to the interaction of the MoS_2 surface with air and moisture, which typically requires several minutes to settle.[23] In contrast, a capping with ~35 nm Al_2O_3 is sufficient to passivate the MoS_2 surface and stabilize the sensor response, now perfectly following the programmed temperature ramp of the heater (stability of over ~2 h, as shown in Figure S3). In fact, Al_2O_3 is known to be an excellent barrier for gas diffusion[24] and has commonly been used for passivation in flexible electronic devices[25] because dense and high-quality films can be obtained at low temperatures[26] that are compatible with flexible plastic substrates.[27] For future application in aqueous or humid environments, the Al_2O_3 passivation could also be applied on the back side of the PI substrate to prevent water vapor diffusion through the PI film.[24,28] We also note that the conductance of the sensors increases by ~50× after Al_2O_3 encapsulation, which can be attributed to the removal of oxygen and water from the surface[23,29] in addition to the n-type doping effects of alumina.[30]

We also estimate the differential TCR and activation energy E_A (see Section S8 in the Supporting Information) by taking the resistance difference immediately before and after the heater stage setting is changed (~4 s for a temperature change of 10 °C) to avoid capturing the slower effects visible for uncapped devices. We find that the absolute TCR and E_A are higher before encapsulation, which indicates that the Fermi level is deeper inside the band gap, as is the case for lower doping. We analyze the conduction mechanism of sensors after encapsulation and deduce that space-charge limited current is present, a common mechanism in lightly doped semiconductors (see Section S9 in the Supporting Information and Figure S5).[31] We also find there are growth-to-growth variations affecting the nonlinearity of the current−voltage characteristics and E_A, indicating differences in doping density: e.g., from variations in sulfur vacancy concentrations (Figure S6).[31,32]

https://doi.org/10.1021/acs.nanolett.2c01344
Nano Lett. 2022, 22, 6135−6140

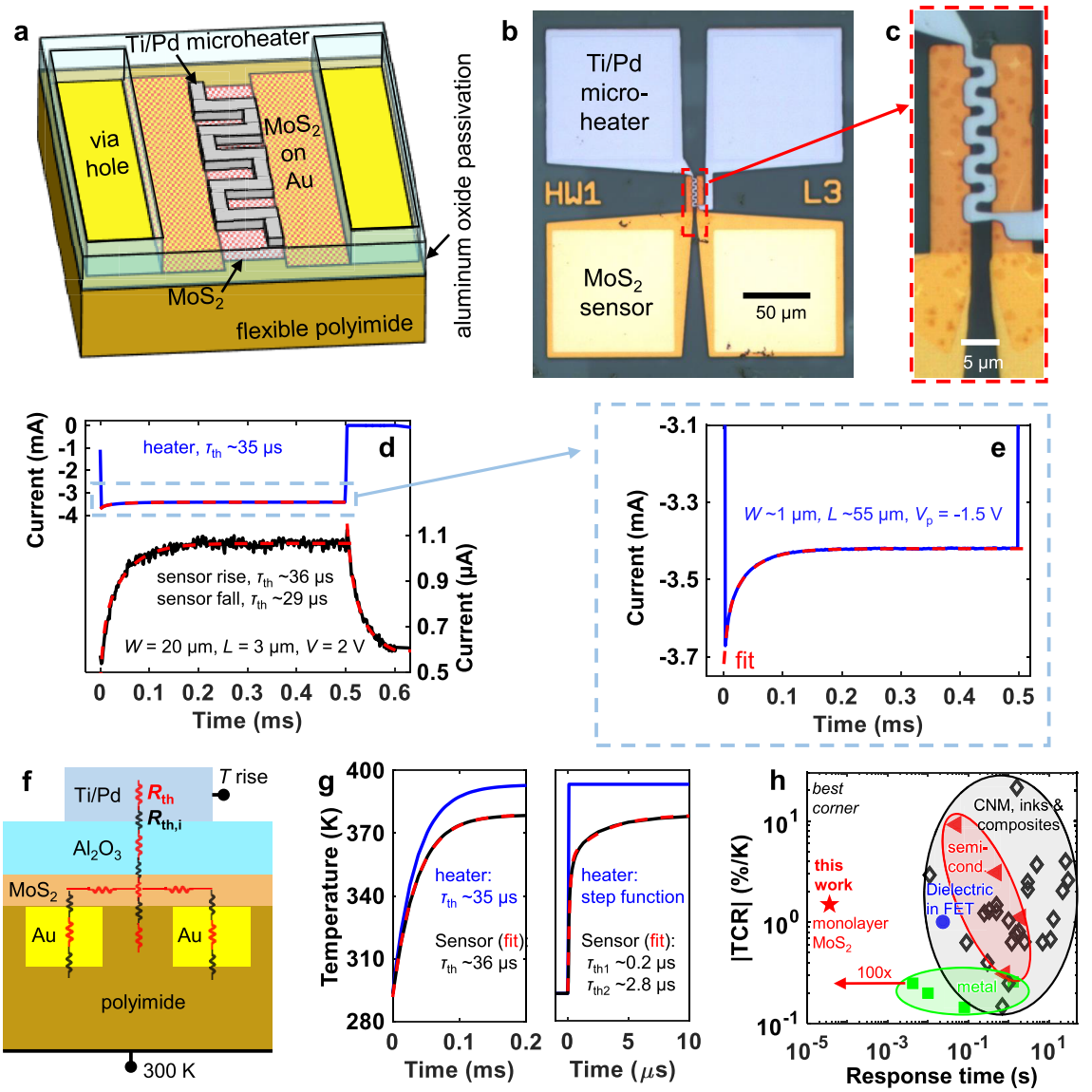

Figure 3. Investigation of sensor response time with integrated microheater structures. (a) Schematic of the metal microheater on top of the temperature sensor. Optical images of (b) the whole structure and (c) the magnified active area with the heater and sensor. (d) Sensor response upon pulsed actuation with the heater. The red dashed lines represent fits with exponential functions (see Section S11 in the Supporting Information). The average thermal time constant τ_{th} of the heater is 35 ± 2 μs. The sensor rise and fall τ_{th} values are 36 ± 2 and 29 ± 2 μs, respectively. We measured five heater−sensor pairs of this geometry to obtain these averages and standard deviations. (e) Enlargement of the transient heater current. (f) Schematic of the thermal simulation. R_{th} and $R_{th,i}$ are the thermal (interface) resistances. (g) Simulated response for a heater with τ_{th} = 35 μs (left) and a step function (right). (h) Benchmarking of flexible temperature sensors. Most sensors have a response time of between 0.1 and 10 s. Thin-film metal sensors have shown the fastest response times down to few milliseconds but generally have a low TCR. Our flexible monolayer MoS_2 sensors have a reasonably high TCR of ∼1.5%/K and ∼100× faster response time in comparison to the fastest metal temperature sensors.

We further investigate the response time of our flexible MoS_2 temperature sensors by fabricating thin metal microheaters (Ti/Pd 3/37 nm) on top of the Al_2O_3 passivation layer (Figure 3a−c). We apply a negative voltage pulse with an amplitude of V_p = −1.5 V, a period of 1 ms, and a 50% duty cycle to the heater while the sensor is direct-current biased with the voltage V = 2 V. We apply a negative V_p to avoid accidentally "turning on" the MoS_2 sensor under the metal heater, because such CVD-grown MoS_2 devices are n-type and in a transistor configuration they turn on with positive gate voltages.[18,22,29,30,32] In Figure 3d, we observe that the MoS_2 sensor current increases when the heater is pulsed, which indicates that the heating dominates. (See additional discussion and data in Section S11 in the Supporting Information.) The sensor is very stable to such pulsed heating, as shown by 1000 cycles in Figure S7. We also obtained similar results with a U-shaped heater without any vertical overlap with the MoS_2 active area, where heat needs to spread laterally to reach the sensor and any possible gating effects are eliminated (Figure S8).

By fitting exponential functions (Section S11 in the Supporting Information) to the heater and the sensor currents, we find that the thermal time constant of the microheater is τ_{th} ≈ 35 μs and the sensor responds with τ_{th} ≈ 36 μs when it is heated and then recovers with τ_{th} ≈ 29 μs. Such heater time constants are common for thin-film metal structures, and the

https://doi.org/10.1021/acs.nanolett.2c01344
Nano Lett. 2022, 22, 6135−6140

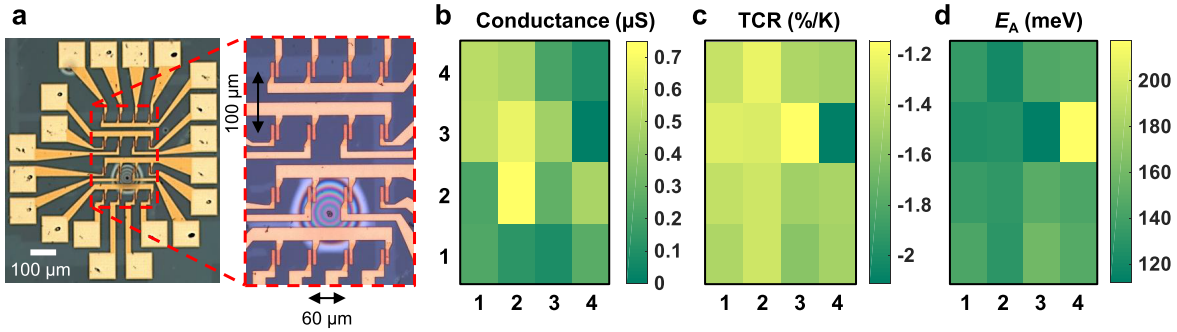

Figure 4. Flexible monolayer MoS_2 temperature sensor arrays with sensors dimensions of $W = 20$ μm and $L = 3$ μm. (a) Optical images of a 4 × 4 sensor array including an enlargement of active sensing region. The concentric feature is a visual artifact from attaching the flexible sensor to a silicon substrate for microscope imaging. Spatial distributions of (b) conductance, (c) temperature coefficient of resistance (TCR), and (d) activation energy E_A. The axis labels represent each sensor index, from 1 to 4. The sensor pitch is ∼60 μm in the horizontal direction and ∼100 μm in the vertical direction.

initial heater current transient shown in Figure 3e (within the first 0.1 ms) can be associated with the positive TCR of the metal.[33] Hence, we can conclude that the heater limits the thermal transients in the system and that the intrinsic speed of our MoS_2 temperature sensors is much faster.

The thermal time constant of an individual MoS_2 monolayer (∼0.615 nm thick) is less than 1 ns, as determined by molecular dynamics simulations.[34] However, the response time of our sensors is limited by the PI substrate, the Al_2O_3 encapsulation, and the thermal resistances of the various material interfaces. To estimate this intrinsic response time of our temperature sensors, we perform thermal simulations (Section S3 in the Supporting Information). We built a 2D cross-sectional structure of our sensors with all involved materials, including their thermal properties and boundary conditions (Figure 3f). Initially, we applied an exponential signal to the heater mimicking the experimental conditions (τ_{th} = 35 μs) and found good agreement in the simulated and experimental sensor time constants (Figure 3g, left). Then, we changed our simulated heater temperature rise to a step function and observed the delay of the simulated sensor response. This indicates that our flexible MoS_2 sensors should be able to react to temperature changes within a few microseconds (Figure 3g, right). Note that a lateral heater offset slightly slows down the sensor response, because this requires additional lateral heat spreading, as confirmed by experiment and simulations in Figure S8. On the other hand, applying heat at the bottom of the PI substrate would slow down the response time to ∼0.5 ms (see Section S12 in the Supporting Information).

Next, we compare the absolute TCR and response time of our devices to those of other flexible temperature sensors (Figure 3h). Many temperature sensors based on carbon nanomaterials (CNM), inks, and composite materials have been investigated with strongly varying TCR values and relatively slow response times of typically between 0.1 and 10 s. Similar results can be found for semiconductor thin films and other types of devices such as temperature-dependent gate dielectrics in field-effect transistors (FETs).[35] The fastest response times for CNMs and semiconductors have been found for poly(vinylidene fluoride)/reduced graphene oxide nanocomposite films (11 ms)[36] and NiO nanoparticles (50 ms),[37] respectively. On the other hand, thin-film metals have shown faster response times down to 4.2 ms[1] but exhibit a limited TCR of ∼0.2−0.3%/K on the basis of their less sensitive mechanism of temperature dependence (electron−phonon scattering[38]). Our atomically thin monolayer MoS_2 temperature sensors on 5 μm PI are ∼100× faster than other flexible temperature sensors on the basis of our experiments (limited by the Ti/Pd microheaters), and we estimate that their intrinsic speed is another order of magnitude higher, through simulations. Table S1 summarizes all literature associated with the data shown in Figure 3h.

Finally, we fabricate and analyze flexible MoS_2 temperature sensor arrays to investigate their suitability for future applications that require spatial mapping of temperature. Figure 4a displays a 4 × 4 array of flexible MoS_2 temperature sensors after fabrication. The color maps in Figure 4b−d illustrate the conductance, TCR, and E_A distributions, respectively, revealing that a 100% yield can be reached with this fabrication and transfer process and that any variation between sensors appears to be random rather than systematic. At the same time, the 16-sensor array does feature one outlier with higher absolute TCR and E_A values in comparison to the other sensors (see Figure S11 for the sensor distributions visualized as bar charts).

In summary, we demonstrated flexible monolayer MoS_2 temperature sensors and arrays with high temperature coefficient of resistance of ∼1−2%/K on 5 μm thin polyimide substrates. All materials used here are biocompatible,[16,39−42] and our temperature sensitivity estimations indicate a suitability for future biomedical applications such as skin or breast cancer detection[11,12] and wound healing,[13] but we note that other use cases may require sensitivity improvements (Section S15 in the Supporting Information). Furthermore, we experimentally determined that the response time of these sensors is <36 μs and our simulations suggest values down to few microseconds, at least 100× shorter than those of other flexible temperature sensors. A fast detection of temperature changes is important to allow a real-time readout in large-scale arrays and, for example, to detect microsecond temperature spikes in power electronics to prevent device failure.[43] Overall, these results pave the way for ubiquitous real-time temperature sensing with atomically thin semiconductors, such as MoS_2.

■ ASSOCIATED CONTENT

Supporting Information

The Supporting Information is available free of charge at https://pubs.acs.org/doi/10.1021/acs.nanolett.2c01344.

https://doi.org/10.1021/acs.nanolett.2c01344
Nano Lett. 2022, 22, 6135−6140

Sample fabrication, measurement setup, field-effect transistor characteristics, light dependence and stability over time, channel vs contact contributions to the device resistance, TCR and E_A extractions, conduction mechanism, thermal time constant measurements and simulations, cycling, simulation details, temperature sensitivity analysis, and array statistics (PDF)

AUTHOR INFORMATION

Corresponding Author

Eric Pop − *Department of Electrical Engineering, Stanford University, Stanford, California 94305, United States; Department of Materials Science & Engineering, Stanford University, Stanford, California 94305, United States;* orcid.org/0000-0003-0436-8534; Email: epop@stanford.edu

Authors

Alwin Daus − *Department of Electrical Engineering, Stanford University, Stanford, California 94305, United States;* Present Address: Chair of Electronic Devices, RWTH Aachen University, 52074 Aachen, Germany; orcid.org/0000-0001-7461-3756

Marc Jaikissoon − *Department of Electrical Engineering, Stanford University, Stanford, California 94305, United States*

Asir Intisar Khan − *Department of Electrical Engineering, Stanford University, Stanford, California 94305, United States;* orcid.org/0000-0003-4635-4667

Aravindh Kumar − *Department of Electrical Engineering, Stanford University, Stanford, California 94305, United States;* orcid.org/0000-0002-4481-9910

Ryan W. Grady − *Department of Electrical Engineering, Stanford University, Stanford, California 94305, United States;* orcid.org/0000-0002-0457-5026

Krishna C. Saraswat − *Department of Electrical Engineering, Stanford University, Stanford, California 94305, United States; Department of Materials Science & Engineering, Stanford University, Stanford, California 94305, United States*

Complete contact information is available at: https://pubs.acs.org/10.1021/acs.nanolett.2c01344

Author Contributions

A.D. conceived the flexible temperature sensors, performed device fabrication and measurements, and analyzed the data. A.I.K. and E.P. conceived the use of ultrathin MoS_2 for temperature sensors. M.J. and A.I.K. performed numerical simulations. A.K. analyzed contact resistance contributions and together with R.W.G. grew the MoS_2 films. A.D., M.J., A.I.K., and E.P. wrote the manuscript. All authors revised and commented on the manuscript. E.P. supervised the work.

Notes

The authors declare no competing financial interest.

ACKNOWLEDGMENTS

A.D. was supported by Beijing Institute of Collaborative Innovation (BICI) and by the National Science Foundation (NSF) Engineering Research Center for Power Optimization of Electro-Thermal Systems (POETS) with Cooperative Agreement No. EEC-1449548. R.W.G. acknowledges a National Science Foundation (NSF) Graduate Research Fellowship. A.I.K. acknowledges a Stanford Graduate Fellowship (SGF). We thank the Stanford Nanofabrication Facility and Stanford Nano Shared Facilities for enabling device fabrication and characterization, funded under NSF award no. ECCS-1542152.

REFERENCES

(1) Webb, R. C.; Bonifas, A. P.; Behnaz, A.; Zhang, Y.; Yu, K. J.; Cheng, H.; Shi, M.; Bian, Z.; Liu, Z.; Kim, Y.-S.; Yeo, W.-H.; Park, J. S.; Song, J.; Li, Y.; Huang, Y.; Gorbach, A. M.; Rogers, J. A. Ultrathin conformal devices for precise and continuous thermal characterization of human skin. *Nat. Mater.* **2013**, *12* (10), 938−944.

(2) Kim, D.-H.; Lu, N.; Ghaffari, R.; Kim, Y.-S.; Lee, S. P.; Xu, L.; Wu, J.; Kim, R.-H.; Song, J.; Liu, Z.; Viventi, J.; de Graff, B.; Elolampi, B.; Mansour, M.; Slepian, M. J.; Hwang, S.; Moss, J. D.; Won, S.-M.; Huang, Y.; Litt, B.; Rogers, J. A. Materials for multifunctional balloon catheters with capabilities in cardiac electrophysiological mapping and ablation therapy. *Nat. Mater.* **2011**, *10* (4), 316−323.

(3) Cherenack, K.; Zysset, C.; Kinkeldei, T.; Münzenrieder, N.; Tröster, G. Woven electronic fibers with sensing and display functions for smart textiles. *Adv. Mater.* **2010**, *22* (45), 5178−5182.

(4) Lee, W. W.; Tan, Y. J.; Yao, H.; Li, S.; See, H. H.; Hon, M.; Ng, K. A.; Xiong, B.; Ho, J. S.; Tee, B. C. A neuro-inspired artificial peripheral nervous system for scalable electronic skins. *Science Robotics* **2019**, *4* (32), No. eaax2198.

(5) Salvatore, G. A.; Sülzle, J.; Dalla Valle, F.; Cantarella, G.; Robotti, F.; Jokic, P.; Knobelspies, S.; Daus, A.; Büthe, L.; Petti, L.; Kirchgessner, N.; Hopf, R.; Magno, M.; Tröster, G. Biodegradable and highly deformable temperature sensors for the internet of things. *Adv. Funct. Mater.* **2017**, *27* (35), 1702390.

(6) Djedidi, O.; Djeziri, M. A.; Benmoussa, S. Remaining useful life prediction in embedded systems using an online auto-updated machine learning based modeling. *Microelectronics Reliability* **2021**, *119*, 114071.

(7) Dodero, A.; Escher, A.; Bertucci, S.; Castellano, M.; Lova, P. Intelligent Packaging for Real-Time Monitoring of Food-Quality: Current and Future Developments. *Applied Sciences* **2021**, *11* (8), 3532.

(8) Lee, J.; Jang, H.; Shin, S.; Jang, K.; Jung, J. In *Over temperature protection in power module for hybrid and electric vehicle*; 2016 IEEE Transportation Electrification Conference and Expo, Asia-Pacific (ITEC Asia-Pacific); IEEE: 2016; pp 432−435. DOI: 10.1109/ITEC-AP.2016.7512992

(9) Yang, F.; Yang, N.; Huo, X.; Xu, S. Thermal sensing in fluid at the micro-nano-scales. *Biomicrofluidics* **2018**, *12* (4), 041501.

(10) Wang, X.; Dong, L.; Zhang, H.; Yu, R.; Pan, C.; Wang, Z. L. Recent progress in electronic skin. *Advanced Science* **2015**, *2* (10), 1500169.

(11) Pirtini Cetingul, M.; Herman, C. Quantification of the thermal signature of a melanoma lesion. *International Journal of Thermal Sciences* **2011**, *50* (4), 421−431.

(12) Zhou, Y.; Herman, C. Optimization of skin cooling by computational modeling for early thermographic detection of breast cancer. *Int. J. Heat Mass Transfer* **2018**, *126*, 864−876.

(13) Fierheller, M.; Sibbald, R. G. A clinical investigation into the relationship between increased periwound skin temperature and local wound infection in patients with chronic leg ulcers. *Advances in Skin & Wound Care* **2010**, *23* (8), 369−379.

(14) Bourne, R. B.; Chesworth, B. M.; Davis, A. M.; Mahomed, N. N.; Charron, K. D. Patient satisfaction after total knee arthroplasty: who is satisfied and who is not? *Clinical Orthopaedics and Related Research* **2010**, *468* (1), 57−63.

(15) Chen, Z.; Zhao, D.; Ma, R.; Zhang, X.; Rao, J.; Yin, Y.; Wang, X.; Yi, F. Flexible temperature sensors based on carbon nanomaterials. *J. Mater. Chem. B* **2021**, *9* (8), 1941−1964.

(16) Chen, X.; Park, Y. J.; Kang, M.; Kang, S.-K.; Koo, J.; Shinde, S. M.; Shin, J.; Jeon, S.; Park, G.; Yan, Y.; MacEwan, M. R.; Ray, W. Z.; Lee, K.-M.; Rogers, J. A.; Ahn, J.-H. CVD-grown monolayer MoS_2 in

bioabsorbable electronics and biosensors. *Nat. Commun.* **2018**, *9* (1), 1690.
(17) Khan, A. I.; Khakbaz, P.; Brenner, K. A.; Smithe, K. K.; Mleczko, M. J.; Esseni, D.; Pop, E. Large temperature coefficient of resistance in atomically thin two-dimensional semiconductors. *Appl. Phys. Lett.* **2020**, *116* (20), 203105.
(18) Daus, A.; Vaziri, S.; Chen, V.; Köroğlu, Ç.; Grady, R. W.; Bailey, C. S.; Lee, H. R.; Schauble, K.; Brenner, K.; Pop, E. High-performance flexible nanoscale transistors based on transition metal dichalcogenides. *Nature Electronics* **2021**, *4*, 495−501.
(19) Smithe, K. K.; Suryavanshi, S. V.; Muñoz Rojo, M.; Tedjarati, A. D.; Pop, E. Low variability in synthetic monolayer MoS_2 devices. *ACS Nano* **2017**, *11* (8), 8456−8463.
(20) Smithe, K. K.; English, C. D.; Suryavanshi, S. V.; Pop, E. Intrinsic electrical transport and performance projections of synthetic monolayer MoS_2 devices. *2D Materials* **2017**, *4* (1), 011009.
(21) Nassiri Nazif, K.; Daus, A.; Hong, J.; Lee, N.; Vaziri, S.; Kumar, A.; Nitta, F.; Chen, M. E.; Kananian, S.; Islam, R.; Kim, K.-H.; Park, J.-H.; Poon, A. S. Y.; Brongersma, M. L.; Pop, E.; Saraswat, K. C. High-specific-power flexible transition metal dichalcogenide solar cells. *Nat. Commun.* **2021**, *12*, 7034.
(22) Kumar, A.; Schauble, K.; Neilson, K. M.; Tang, A.; Ramesh, P.; Wong, H.-S. P.; Pop, E.; Saraswat, K. In *Sub-200 Ω·μm alloyed contacts to synthetic monolayer MoS_2*; IEEE International Electron Devices Meeting (IEDM), IEEE, :2021; pp 7.3.1−7.3.4. DOI: 10.1109/IEDM19574.2021.9720609
(23) Late, D. J.; Huang, Y.-K.; Liu, B.; Acharya, J.; Shirodkar, S. N.; Luo, J.; Yan, A.; Charles, D.; Waghmare, U. V.; Dravid, V. P.; Rao, C. N. R. Sensing behavior of atomically thin-layered MoS_2 transistors. *ACS Nano* **2013**, *7* (6), 4879−4891.
(24) Carcia, P. F.; McLean, R.; Reilly, M.; Groner, M.; George, S. Ca test of Al_2O_3 gas diffusion barriers grown by atomic layer deposition on polymers. *Appl. Phys. Lett.* **2006**, *89* (3), 031915.
(25) Daus, A.; McClellan, C. J.; Schauble, K.; Costa, J. C.; Grady, R. W.; Petti, L.; Cantarella, G.; Münzenrieder, N.; Pop, E. In *Aluminum oxide as a dielectric and passivation layer for (flexible) metal-oxide and 2D semiconductor devices, Oxide-based Materials and Devices XII*; International Society for Optics and Photonics: 2021; p 116871I. DOI: 10.1117/12.2587997
(26) Groner, M.; Fabreguette, F.; Elam, J.; George, S. Low-temperature Al_2O_3 atomic layer deposition. *Chem. Mater.* **2004**, *16* (4), 639−645.
(27) Nathan, A.; Ahnood, A.; Cole, M. T.; Lee, S.; Suzuki, Y.; Hiralal, P.; Bonaccorso, F.; Hasan, T.; Garcia-Gancedo, L.; Dyadyusha, A.; Haque, S.; Andrew, P.; Hofmann, S.; Moultrie, J.; Chu, D.; Flewitt, A. J.; Ferrari, A. C.; Kelly, M. J.; Robertson, J.; Amaratunga, G. A.; Milne, W. I. Flexible electronics: the next ubiquitous platform. *Proceedings of the IEEE* **2012**, *100*, 1486−1517.
(28) Schaubroeck, D.; Verplancke, R.; Cauwe, M.; Cuypers, D.; Baumans, K.; Op de Beeck, M. In *Polyimide-ALD-polyimide layers as hermetic encapsulant for implants*, XXXI International Conference on Surface Modification Technologies (SMT31), 2017; pp 1−6. http://hdl.handle.net/1854/LU-8526723
(29) Qiu, H.; Pan, L.; Yao, Z.; Li, J.; Shi, Y.; Wang, X. Electrical characterization of back-gated bi-layer MoS_2 field-effect transistors and the effect of ambient on their performances. *Appl. Phys. Lett.* **2012**, *100* (12), 123104.
(30) McClellan, C. J.; Yalon, E.; Smithe, K. K.; Suryavanshi, S. V.; Pop, E. High Current Density in Monolayer MoS_2 Doped by AlO_x. *ACS Nano* **2021**, *15* (1), 1587−1596.
(31) Röhr, J. A.; MacKenzie, R. C. Analytical description of mixed ohmic and space-charge-limited conduction in single-carrier devices. *J. Appl. Phys.* **2020**, *128* (16), 165701.
(32) Kim, I. S.; Sangwan, V. K.; Jariwala, D.; Wood, J. D.; Park, S.; Chen, K.-S.; Shi, F.; Ruiz-Zepeda, F.; Ponce, A.; Jose-Yacaman, M.; Dravid, V. P.; Marks, T. J.; Hersam, M. C.; Lauhon, L. J. Influence of stoichiometry on the optical and electrical properties of chemical vapor deposition derived MoS_2. *ACS Nano* **2014**, *8* (10), 10551−10558.
(33) Zhou, Q.; Sussman, A.; Chang, J.; Dong, J.; Zettl, A.; Mickelson, W. Fast response integrated MEMS microheaters for ultra low power gas detection. *Sensors and Actuators A: Physical* **2015**, *223*, 67−75.
(34) Suryavanshi, S. V.; Gabourie, A. J.; Farimani, A. B.; Pop, E. Thermal boundary conductance of two-dimensional MoS_2 interfaces. *J. Appl. Phys.* **2019**, *126* (5), 055107.
(35) Mandal, S.; Banerjee, M.; Roy, S.; Mandal, A.; Ghosh, A.; Satpati, B.; Goswami, D. K. Organic field-effect transistor-based ultrafast, flexible, physiological-temperature sensors with hexagonal barium titanate nanocrystals in amorphous matrix as sensing material. *ACS Appl. Mater. Interfaces* **2019**, *11* (4), 4193−4202.
(36) Park, J.; Kim, M.; Lee, Y.; Lee, H. S.; Ko, H. Fingertip skin−inspired microstructured ferroelectric skins discriminate static/dynamic pressure and temperature stimuli. *Science Advances* **2015**, *1* (9), No. e1500661.
(37) Shin, J.; Jeong, B.; Kim, J.; Nam, V. B.; Yoon, Y.; Jung, J.; Hong, S.; Lee, H.; Eom, H.; Yeo, J.; Choi, J.; Lee, D.; Ko, S. H. Sensitive wearable temperature sensor with seamless monolithic integration. *Adv. Mater.* **2020**, *32* (2), 1905527.
(38) Cheng, Z.; Liu, L.; Xu, S.; Lu, M.; Wang, X. Temperature dependence of electrical and thermal conduction in single silver nanowire. *Sci. Rep.* **2015**, *5*, 10718.
(39) Constantin, C. P.; Aflori, M.; Damian, R. F.; Rusu, R. D. Biocompatibility of polyimides: A mini-review. *Materials* **2019**, *12* (19), 3166.
(40) Finch, D. S.; Oreskovic, T.; Ramadurai, K.; Herrmann, C. F.; George, S. M.; Mahajan, R. L. Biocompatibility of atomic layer-deposited alumina thin films. *Journal of Biomedical Materials Research A* **2008**, *87A*, 100−106.
(41) Matarèse, B. F.; Feyen, P. L.; Falco, A.; Benfenati, F.; Lugli, P.; deMello, J. C. Use of SU8 as a stable and biocompatible adhesion layer for gold bioelectrodes. *Sci. Rep.* **2018**, *8*, 5560.
(42) Sidambe, A. T. Biocompatibility of advanced manufactured titanium implants—A review. *Materials* **2014**, *7* (12), 8168−8188.
(43) Ciappa, M.; Castellazzi, A. In *Reliability of high-power IGBT modules for traction applications*; 2007 IEEE International Reliability Physics Symposium Proceedings. 45th Annual; IEEE: 2007; pp 480−485. DOI: 10.1109/RELPHY.2007.369938

https://doi.org/10.1021/acs.nanolett.2c01344
Nano Lett. 2022, 22, 6135−6140

Supporting Information

Fast-Response Flexible Temperature Sensors with Atomically Thin Molybdenum Disulfide

Alwin Daus[#,†], *Marc Jaikissoon*[#], *Asir Intisar Khan*[#], *Aravindh Kumar*[#], *Ryan W. Grady*[#], *Krishna C. Saraswat*[#,‡], *Eric Pop*[#,‡,*]

#Department of Electrical Engineering, Stanford Univ., Stanford, CA 94305, U.S.A.

‡Department of Materials Science & Engineering, Stanford Univ., Stanford, CA 94305, U.S.A.

†Present address: Chair of Electronic Devices, RWTH Aachen University, 52074 Aachen, Germany

[*]Corresponding author, email: epop@stanford.edu

Section S1: Device Fabrication

The fabrication and transfer process has been described in detail in our recent work including additional analysis of MoS_2 material and structures before/after transfer.[1] Here, the temperature sensors have been fabricated based on the same approach as described briefly in the following: First, monolayer MoS_2 was grown by chemical vapor deposition onto SiO_2/Si substrates with methods described in detail elsewhere.[2, 3] Then, 45 nm thick Au contacts were electron-beam evaporated at a rate of 0.5 Å/s and patterned via optical lithography and lift-off. The lift-off process is described in detail in ref. [1]. Next, the MoS_2 was patterned by reactive ion etching using CF_4:O_2 gas at a flow ratio of 50:10 sccm (power: 100 W, pressure: 30 mTorr, time: 30 s). This was followed by an *in situ* surface cleaning with O_2 plasma (power: 20 W, pressure: 10 mTorr, gas flow: 40 sccm, time: 30 s), where the MoS_2 active area remained protected by photoresist. Afterwards, contact leads and pads were electron-beam evaporated (Au/Ti, thicknesses: 60/5 nm, deposition rates: 0.5/0.1 Å/s), and patterned via optical lithography and lift-off. Then, 5 µm thick polyimide (PI) (PI-2610, HD MicroSystems) was spin-coated on top, baked hot plates at 90 °C and 150 °C for each 90 s, and subsequently cured in a nitrogen oven at 250 °C for 30 min. After that, the Au and MoS_2 features, embedded into PI, were simply released by actuation in deionized water as described in ref. [1].

After transfer, the MoS_2 surface was passivated by first electron-beam evaporating a 1.5 nm aluminum seed layer (rate: 0.2 Å/s) and then thermal atomic-layer deposition (300 cycles, precursors: trimethylaluminum and water) at 200 °C leading to a total thickness of ~35 nm. Finally, the contact pads were opened by aluminum etchant at 40 °C (J.T. Baker Aluminum etch 16-1-1-2,

etch time: 13 min). The photoresist mask for the contact pad etch was defined by optical lithography on the released polyimide as described previously.[4] This concluded the temperature sensor fabrication. For the integration of microheaters on top of the temperature sensors (Figures 3, S8), we performed one additional optical lithography step and lift-off to pattern 3/37 nm Ti/Pd (electron-beam evaporated at rates of 0.1/0.5 Å/s) on top of aluminum oxide.

Section S2: Electrical measurements

Temperature profiles with Linkam stage: We characterized the temperature sensors by mounting a Linkam stage (model THMS600 with T95 system controller) to a probe station in ambient air and performed measurements in the dark. For the staircase temperature measurements shown in Figure 2 we programmed steps of 27, 35, 45, 55, 65, 75, 85 °C with a hold time of each 30 s and a ramp rate of 150 °C/min (when the temperature changes). The temperature of the stage settles quickly without any noticeable overshoot, as visible for the sensor response in Figure 2b. For the current-voltage sweeps in Figure S5a, we instead held the temperatures constant for ~5 min before running the measurement. The electrical data were collected with a Keithley 4200 system using source-measure units.

Microheater measurements: The samples were measured on a probe station in ambient air and in the dark. We used pulse-measure units on a Keithley 4200 system to perform the synchronized measurements of heaters and sensors.

Section S3: Numerical simulations

We performed 2D transient electro-thermal simulations using COMSOL™ Multiphysics with the device geometry shown in Figure 3f. The input transient temperature pulse accountable for the temperature rise in the simulation is defined by an exponential function with a time constant of 35 µs obtained from our experimental measurement or as a step function (see Figure 3g). As indicated in Figure 3f, we have placed the heater vertically aligned on top of the sensor in the simulation which represents a heater right on top of the sensor similar to our experimental setup with a meander heater. For our U-shaped heater geometry (Figure S8), we instead used a lateral offset in the 2D simulation with a distance of 500 nm from the Au contacts which represents the experimental situation. The simulation domain takes all material electrical (resistivity, ρ) and thermal characteristics (thermal conductivity, k) as well as the thermal boundary resistances (TBR) present at the material pair interfaces as the main input parameters. The thermal conductivities of the materials used in the simulations and the thermal boundary resistances (TBR) of material pairs are detailed elsewhere (see Supplementary Table 1 in our prior work[1]). Reasonable estimates are assumed in the case of parameters not directly reported in the literature.

We assumed isothermal boundary condition at the bottom interface of the PI substrate at $T = 300$ K. On the outer circumference open boundary conditions were assumed, so that the heat can flow out of the domain (at $T = 300$ K) or into the domain. At the top boundary, a convective heat flux boundary condition was assumed conforming to the device measurement condition (ambient air). 1 µm thick PI was used in the simulation because the temperature profile already reaches room temperature within a depth of a few hundred nanometers in the PI.

Section S4: Field-effect transistor characteristics

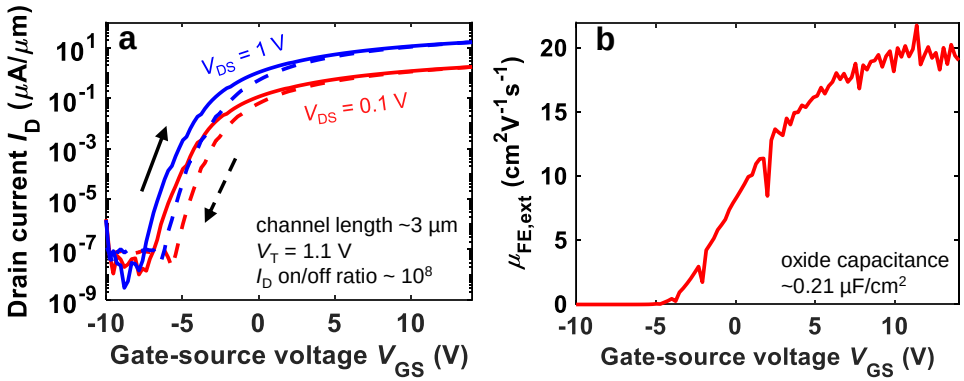

Figure S1. Characteristics of a Ti/Pd top-gated MoS_2 field-effect transistor fabricated within the same process as the temperature sensors with Ti/Pd microheaters. The Al_2O_3 capping layer acts as gate dielectric. The characteristics are comparable to prior work.[1] (a) Transfer characteristics at two different drain-source voltages V_{DS}. The high I_D on/off ratio and low hysteresis indicate good quality of MoS_2 and its interfaces. (b) Extrinsic field-effect mobility $\mu_{FE,ext}$ as a function of V_{GS}.

Figure S1 confirms good quality of the MoS_2 used in this study consistent with prior works.[1-3] Here, we discuss how the quality may impact the sensor behavior. The crystallinity and grain size will have an influence on the transport mechanism. We have determined ohmic and space-charge limited current (see Section S9), which have an Arrhenius temperature behavior and require sufficient degree of crystallinity for band-like transport within MoS_2. In contrast, a large number of grain boundaries (e.g., in nanocrystalline material) and high defect density could lead to different conduction mechanisms like variable range hopping,[5,6] which have a different temperature dependence. High defectivity would also lead to higher overall resistivity, which could influence sensitivity as discussed in Section S15. However, small crystal grains could reduce variability in arrays because the number of grain boundaries will be statistically averaged. Differences in doping of MoS_2 will also affect the conduction mechanism and thus temperature coefficient of resistance (TCR).[6, 7] The thermal time constant of the sensors is not expected to be affected by material quality because the thermal properties of the overall device are dominated by interfaces and packaging.

Section S5: Drift after illumination with the microscope light

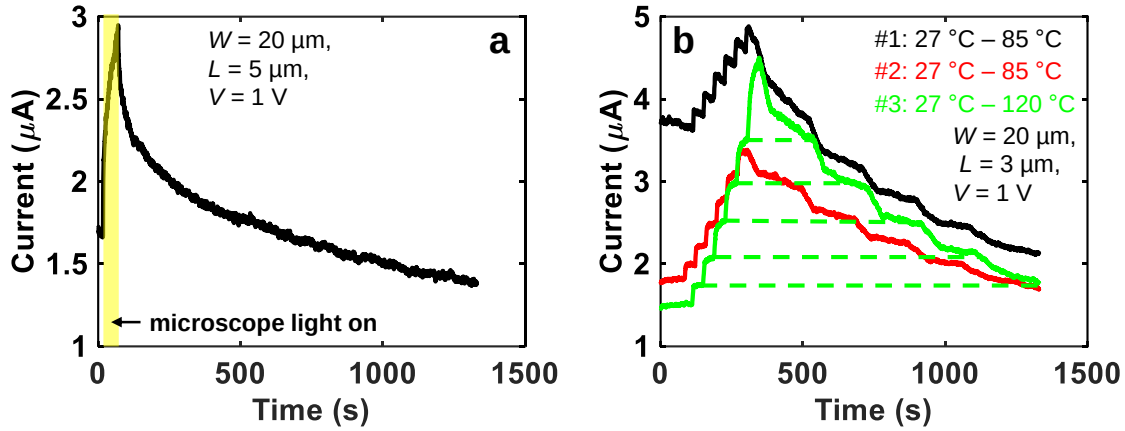

Figure S2. Drift after illumination with microscope light. (a) Current vs. time in a temperature sensor at room temperature where the light was switched on for ~50 s as indicated in yellow. The recovery to similar current levels takes ~15 minutes. (b) Measurements in dark right after the microscope light was switched on and off for probing the sensor. There is a large baseline drift for the first measurement. The horizontal lines indicate that similar current levels are reached for cooling down compared to heating up of the heater stage for the third measurement. We allow for longer times for the cooling because the cooling rate (passive) is much slower than the heating rate (active). As discussed in the main manuscript, the drift can also be eliminated by an initial 15-20 min anneal at 120 °C after probing. *W*, *L* denote the width and length of the sensor, and *V* the applied voltage.

Section S6: Sensor current stability

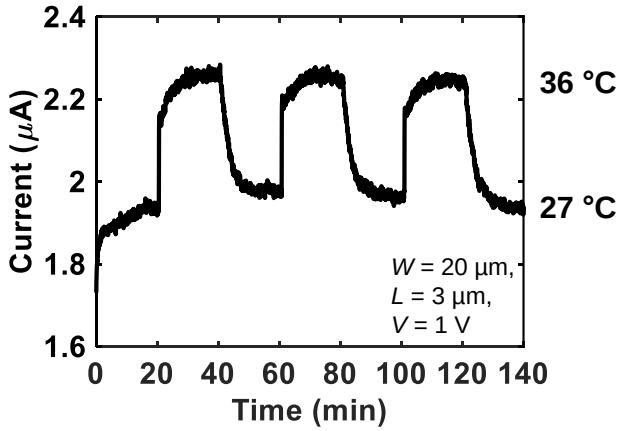

Figure S3. Current vs. time for a measurement over >2 hours where the temperature of the heater stage was changed multiple times between 27 °C and 36 °C (hold time each 20 min). *W*, *L* denote the width and length of the sensor, and *V* the applied voltage.

Section S7: Channel vs. contact contributions to the device resistance

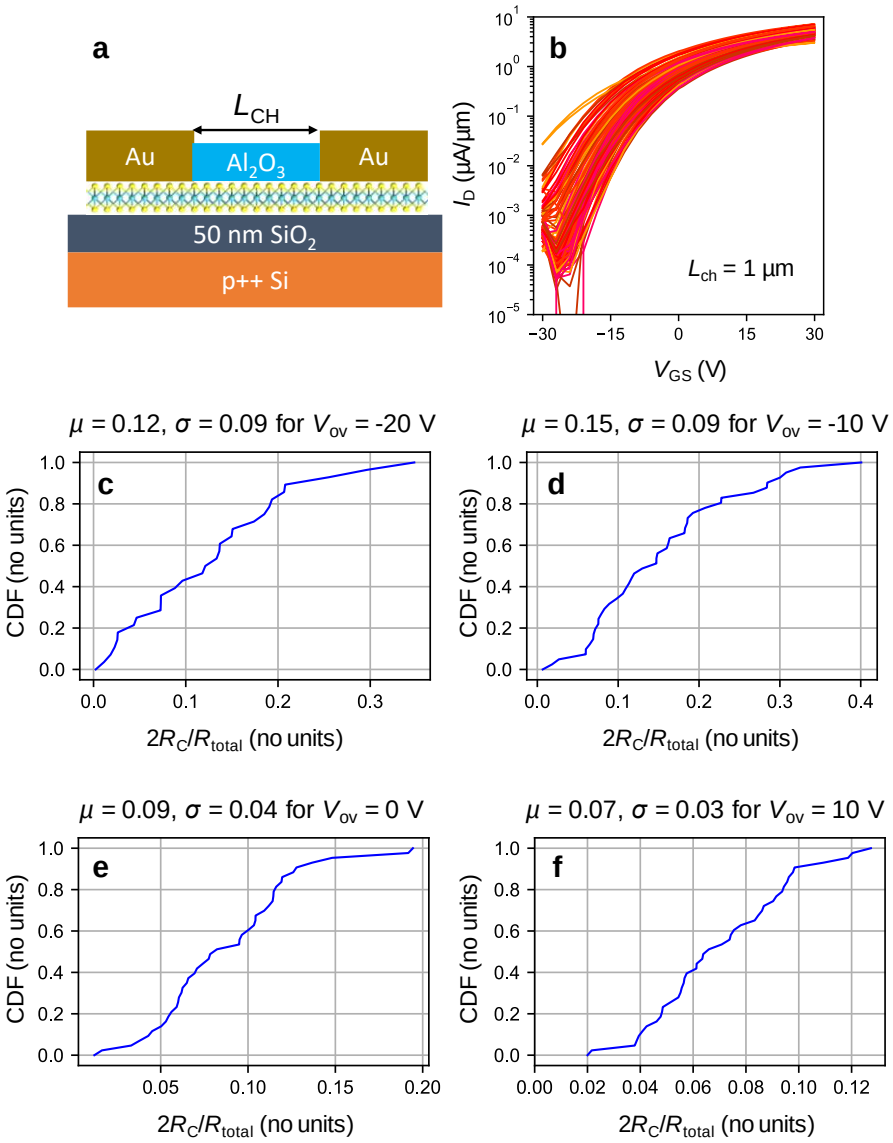

Figure S4. Study of contact resistance R_C for monolayer MoS_2 with Au contacts, Al_2O_3 capping and different doping levels controlled electrostatically with a global back-gate (p^{++} Si). The study is based on transmission line method (TLM) analysis where the channel length L_{CH} shown in the schematic cross-section in (a) is varied from 100 nm to 1 μm.[8] The exemplary drain current I_D vs. gate-source voltage V_{GS} characteristics for devices L_{CH} = 1 μm from ~40 TLMs are displayed in (b). Cumulative density function (CDF) vs. resistance ratio ($2R_C/R_{total}$) calculated at L_{CH} = 3 μm at an overdrive voltage V_{ov} (= V_{GS} - threshold voltage) of (c) -20 V, (d) -10 V, (e) 0 V and (f) 10 V. μ and σ denote the median and standard deviation for each distribution. The resistance ranges in our flexible MoS_2 temperature sensors indicate that $V_{ov} \approx$ -20 V corresponds to similar doping levels, thus the contact resistance contributes ~12% to the total resistance at L_{CH} = 3 μm and our device behavior is dominated by the MoS_2 channel rather than by any contact effects.

Section S8: Extraction of the differential temperature coefficient of resistance (TCR) and activation energy E_A.

We extract the differential TCR (%/K) from the resistances R at the temperatures T (K) as follows:

$$TCR_i = \frac{R_i - R_{i-1}}{R_{i-1}(T_i - T_{i-1})} \times 100$$

Similarly, we extract the differential E_A (meV) from the current I (A) at T:

$$E_{A,i} = \frac{\ln(I_i) - \ln(I_{i-1})}{1/T_i - 1/T_{i-1}} \times (-k_B) \times 1000$$

where k_B denotes the Boltzmann constant.

Section S9: Analysis of the conduction mechanism in MoS_2

To analyze the conduction mechanism in our MoS_2 sensors, we performed current-voltage (*I-V*) measurements at different temperatures. We analyze this in 2-point configuration as this is how we operate our sensors throughout this work. Our prior works[1, 8] have indicated that micron-scale devices with Au contacts are typically channel-dominated rather than contact-dominated, which we have confirmed in our analysis in Section S7.

The *I-V* characteristics can vary from growth-to-growth but in general they have a more or less pronounced non-linear component with a slope >1 (Figures S5a and S6a). This can be related to variations in doping concentration, because it is expected that high doping will lead to a more ohmic type conduction ($I \propto V$) where free carriers in the semiconductor dominate and low doping (or intrinsic) semiconductors would rely more on conduction from carriers injected by the contacts also known as space-charge limited current (SCLC, $I \propto V^2$).[9] Note, that the carrier injection does not depend on the properties of the contacts (as long as symmetric contacts are used, as is the case here).[10, 11] In SCLC, the contacts supply a sufficiently large reservoir of carriers prepared to enter the semiconductor as required, which leads to the formation of a virtual cathode within the semiconductor.[11] Both SCLC and ohmic conduction have an Arrhenius type (exponential) temperature dependence, which has commonly been observed for MoS_2 at high temperature >100 K.[5, 6, 12-14] The exponential resistance-temperature relationship and the Arrhenius plots for E_A extraction are shown in Figure S5b,c, respectively. Figure S5d displays the voltage dependence of E_A known to occur for SCLC.[12, 14, 15] Figure S6 compares two different growths revealing differences in non-linearity of the *I-V* curves. In accordance, E_A is lower for the device with higher *I-V* linearity indicating that the Fermi level is closer to the conduction band (Figure S6b).[5, 12, 15]

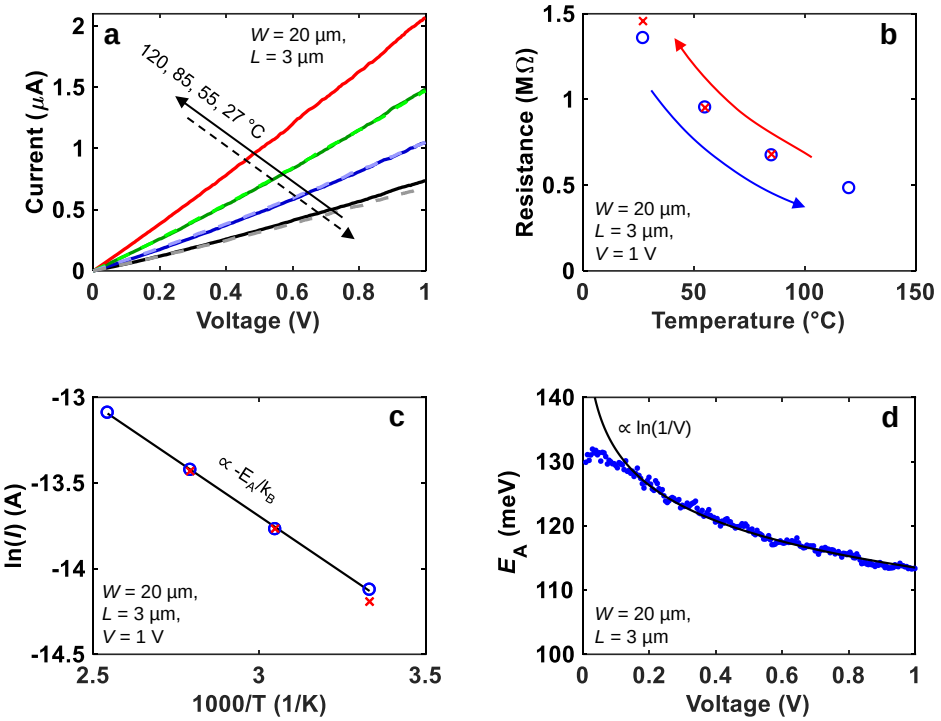

Figure S5. Analysis of conduction mechanism. (a) Current-voltage characteristics of the sensors at different temperatures. (b) Resistance vs. temperature at a voltage $V = 1$ V. (c) Arrhenius plot with a fit (solid line) for E_A. (d) E_A vs V plot showing a $\ln(1/V)$ dependence. W, L denote the width and length of the sensor.

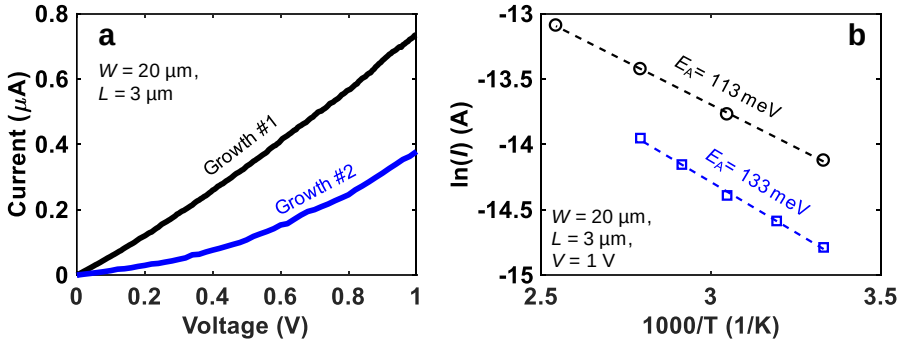

Figure S6. Comparison of two different growths. (a) Current-voltage characteristics of the sensors at 27 °C. (b) Arrhenius plot. W, L denote the width and length of the sensor, and V the applied voltage.

Section S10: Temperature cycling with integrated microheater

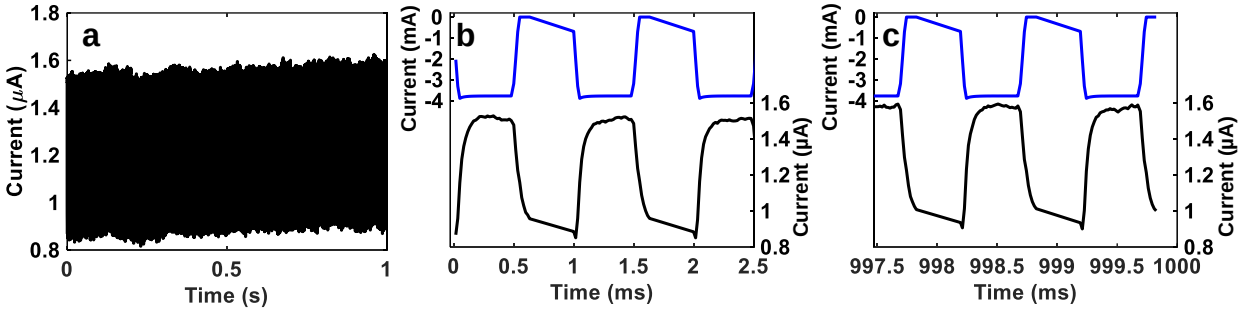

Figure S7. Temperature sensor subjected to 1000 heating cycles with an integrated microheater. The heater geometry and pulse parameters are the same as in Figure 3. (a) Sensor response for all 1000 cycles. First (b) and last (c) few cycles shown for both heater (top, blue) and sensor (bottom, black).

Section S11: Measurements with microheaters and thermal time constant extraction

We extract the thermal time constant τ_{th} based on an exponential function:

$$I = a\left(1 - e^{\frac{-t}{\tau_{th1}}}\right) + b\left(1 - e^{\frac{-t}{\tau_{th2}}}\right) + c$$

The current I (or temperature T for numerical simulations) is fitted as a function of time t with a, b, c, τ_{th1} and τ_{th2} as fitting parameters. Note, in most cases a single exponential function suffices (therein time constant denoted as $\tau_{th} = \tau_{th1}$), where we set $b = 0$. Only for the simulated step response we need the double-exponential function to obtain a satisfactory fitting result.

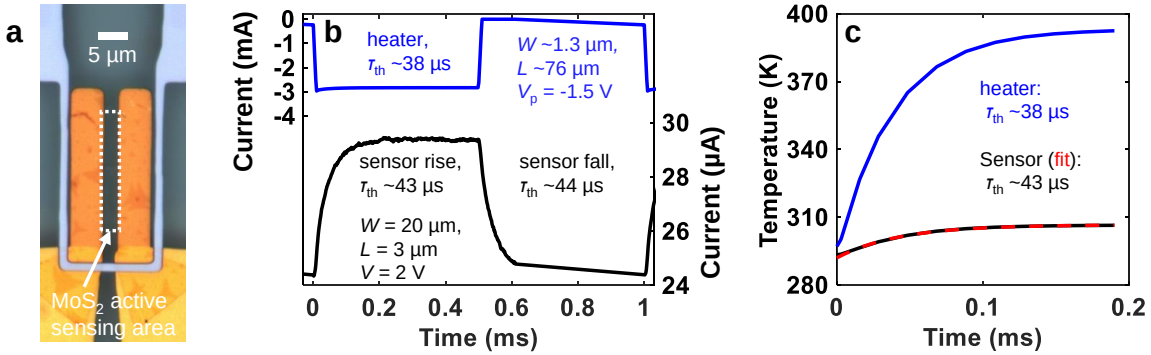

Figure S8. (a) Microscope image of U-shaped microheater surrounding the MoS_2 active sensing area. (b) Electrical measurement. The average thermal time constant τ_{th} of the heater is 38 ± 2 µs. The sensor rise and fall τ_{th} are 43 ± 4 µs and 44 ± 4 µs, respectively. We measured 4 heater-sensor pairs of this geometry to obtain these averages and standard deviations. (c) Simulation with lateral heater/sensor offset of 500 nm from the Au electrodes, similar as shown in (a). The simulation reproduces a comparable temporal response as in the experiment. Noteworthy, the temperature rise is much smaller for a heater with lateral offset compared to a heater vertically aligned with the sensor, which is also visible in the experiment based on much lower relative changes in current magnitude (compare to Figure 3d,g). The higher sensor current (pre-heated) here compared to Figure 3 stems from the growth-to-growth variations discussed in the manuscript and Figure S6.

Discussion on possible electrostatic gating effects of the microheaters:

To investigate simultaneous gating and heating effects in the vertically-overlapped microheater-sensor structures, we also looked at periodic heater actuation with a sinusoidal signal. For this, we used a separate measurement setup, where an arbitrary pulse function generator (Agilent 81160A) was used to supply the sinusoidal signal to the heater. At the same time, the sensor was dc biased at 1 µA with a Keithley 4200 system. The alternating current (ac) sensor response was measured through a low-noise voltage preamplifier (SR560, Stanford Research Systems) which was used to filter the dc component before display on an oscilloscope (Agilent MSO7104A). The resulting waveforms are displayed in Figure S9a. The sensor shows minima when the heater voltage is at its positive and negative peaks, which is expected for Joule heating because it is not polarity-dependent. This indicates that the heating effect dominates, because electrostatic gating alone would cause a sensor voltage peak in the opposite direction (positive) when the heater voltage has its negative peak (depleting MoS_2 of carriers). The electrostatic gating and Joule heating effects can be separated by performing a Fast-Fourier-Transformation (FFT) on the temporal sensor data (Figure S9b). In agreement with this discussion, we find that the 1-frequency (1-*f*, gating) amplitude is smaller than the 2-frequency (2-*f*, heating) amplitude.

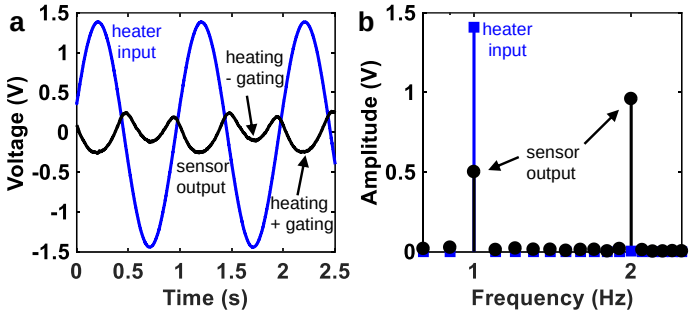

Figure S9. Sinusoidal heater actuation of the heater-sensor configuration shown in Figure 3. (a) The heater input is modulated with a frequency $f = 1$ Hz. The sensor output shows minima when the heater voltages are both at maximum or minimum. When heater voltages are positive, the effects of heating and gating are effectively added, while at negative heater voltages the effects subtract from each other. (b) Fast-Fourier Transformation (FFT) of heater and sensor data showing the 1 Hz actuation of the heater (1-*f* component) and the 1-*f* and 2-*f* sensor components attributed to gating and Joule heating, respectively. The higher amplitude of the 2-*f* component in the sensor indicates that Joule heating dominates over gating in sensors using the metal microheater.

It has to be noted here that the sinusoidal measurement is not suitable to measure τ_{th} of the sensors because the intrinsic τ_{th} of the heater (Figure 3e) skews the signal, especially when increasing the frequency. Thus, the electrostatic gating and Joule heating cannot be fully separated in this structure. However, we do not believe that the extraction of τ_{th} from the pulsed measurement (Figure 3) is affected by electrostatic gating (as discussed in Section S4). To support this, we have also performed the above measurement (Figure S8) where the microheater is laterally offset by several microns from the active sensing area, thereby eliminating any gating effects. The slightly slower τ_{th} (~43 µs) can be attributed to additional lateral heat spreading necessary before reaching the sensors. The fact that our purely thermal simulations match well the temporal responses of our sensors for both types of heater locations (on top and laterally offset), supports the conclusion that electrostatic effects do not disturb the extraction of τ_{th}.

Section S12: Thermal time constant for heating through the polyimide substrate

In our experiment, we cannot determine the thermal time constant when heating is performed through the PI substrate, because the speed of our heater stage is limited to 150 °C/min and our sensors can react much faster than that (Section S2 and Figure 2). Thus, we use our numerical simulation approach (Section S3) to determine the expected time constant for heating from the bottom of the ~5 µm thick PI substrate (see Figure S10).

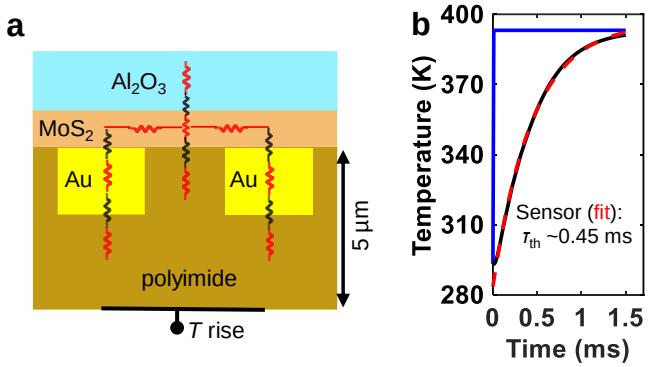

Figure S10. Simulated transient thermal behavior when the heat source is at the bottom of the ~5 µm thick PI substrate. (a) Schematic of the simulated structure. (b) Sensor temperature change when a temperature step of 100 K (blue) is applied to the bottom of the PI. The red dashed line represents the fit from which we estimate a thermal time constant of ~0.45 ms, which is much slower than heating from the top (compare to Figure 3).

Section S13: Benchmarking

Material and reference	TCR (%/K)	Time constant (s)
Magnesium[16]	0.2	10^{-2}
Chromium/Gold[17]	0.25	4.2×10^{-3}
hexagonal barium titanate nanocrystals dielectric[18]	-1	2.4×10^{-2}
NiO nanoparticles[19]	-9.2	5×10^{-2}
Graphene (Gr) nanowalls[20]	21.4	1.6
Silk-nanofiber-derived carbon fiber membranes[21]	-0.81	1.8
Carbon nanotubes (CNTs)/PEDOT:PSS[22]	-0.25	1
Reduced graphene oxide (r-GO)[23]	0.63	1.2
poly(*N*-isopropylacrylamide) (pNIPAM)/PEDOT:PSS/CNT[24]	-2.6	30
Vanadium dioxide (VO_2)[25]	-1.12	2
Graphene nanoribbon (GNR) ink[26]	1.27	5×10^{-1}
Printed multi-walled CNT[27]	-1.04	1
Platinum[28]	0.145	8×10^{-2}
Printed PEDOT:PSS[29]	-0.77	1.5
Gr nanoplatelets (GNP)[30]	3.71	5

Gr monolayer doped by polyvinylidene fluoride-trifluoroethylene (PVDF-TrFE) nanocomposites[31]	2.5	3
Gr/Nickel[32]	1.08	13
Polyethyleneimine (PEI)/r-GO[33]	1.3	3.3×10^{-1}
Gr hydrogel[34]	2.04	22
CNT/PEDOT:PSS[35]	0.64	2.5
CNT/ionic liquid[36]	-1.23	2.5×10^{-1}
CNT[36]	-0.4	3×10^{-1}
Gr[36]	-2.11	3
Gr[36]	-1.48	5×10^{-1}
r-GO[36]	-0.63	1.2
r-GO[36]	-1.3	3.3×10^{-1}
CNT/PEDOT:PSS[36]	-0.63	9×10^{-2}
Gr/PEDOT:PSS[36]	-0.06	18
r-GO fiber[36]	-0.64	7
Graphite/polyethylene oxide (PEO)/ poly(vinylidene fluoride) (PVDF)[36]	4	26
CNT/PEDOT:PSS field-effect transistor[36]	0.68	11
polysilicon[37]	-0.31	8×10^{-1}
Gold/Titanium[38]	0.26	1.3
Polyvinyl/carbon black[39]	-0.15	7×10^{-1}
Vanadium dioxide (VO_2)[40]	-3.1	5×10^{-1}
r-GO/PVDF[41]	2.93	1.1×10^{-2}

Table S1. Benchmarking of flexible temperature sensors with various sensing materials.

Section S14: Sensor statistics in a 4x4 array

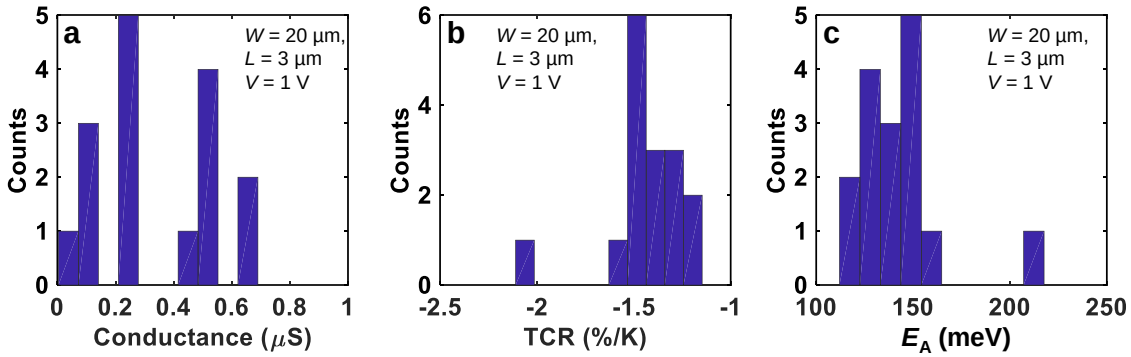

Figure S11. Bar charts representing the distribution in 4x4 flexible monolayer MoS_2 sensor arrays. (a) Conductance. (b) Temperature coefficient of resistance (TCR) and (c) Activation energy E_A, both measured over the 27 °C to 85 °C temperature range.

Section S15: Temperature sensitivity analysis

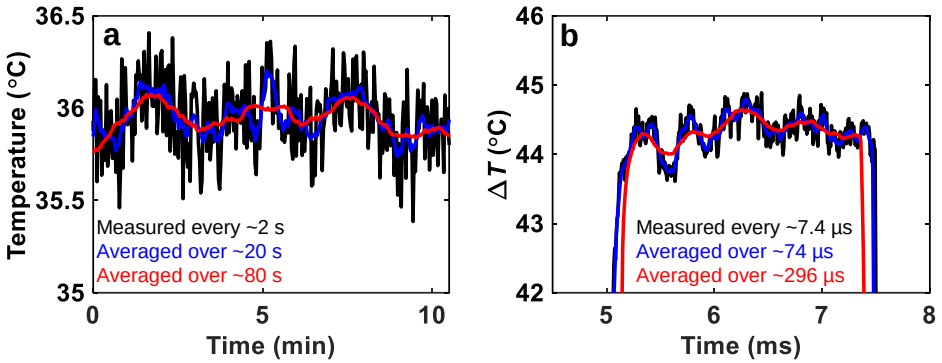

Figure S12. Measurement fluctuations at constant temperature. The measured current was converted to temperature using a typical TCR value of -1.5 %/K. (a) The data are converted from a direct-current (dc) measurement where the PI substrate was heated from the backside as described in the first part of Section S2. The heater setpoint was 36 °C which matches well with the TCR used for converting sensor current to temperature. The dc data were measured every 2 s (Keithley 4200 settings: delay factor = 1.3, filter factor = 3, A/D Aperture time = auto, interval = 0.3 s, hold time = 0 s). The peak-to-peak temperature variations for unaveraged data (black) and averaging over 10 (blue) and 40 (red) data points reveal detectable temperature changes of ~1.13 °C ± 0.14 °C, ~0.60 °C ± 0.17 °C, and ~0.25 °C ± 0.06 °C, respectively (averaged over 3 measurements ~10 min each). (b) The data are converted from a pulsed measurement where a microheater on top of Al_2O_3/MoS_2 is used as described in the second part of Section S2. There is no external verification of the temperature possible and thus the temperature difference ΔT shown here is based on the pre-heated resistance and the abovementioned TCR. The data is collected in time steps of ~7.4 µs. The peak-to-peak temperature variations for unaveraged data (black) and averaging over 10 (blue) and 40 (red) data points reveal detectable temperature changes of ~1.35 °C ± 0.15 °C, ~0.95 °C ± 0.21 °C, and ~0.57 °C ± 0.17 °C, respectively (averaged over 7 measurements ~2.5 ms each).

As described in Figure S12, the peak-to-peak temperature variations range from about 1.4 °C to 0.25 °C, depending on the measurement setup and the amount of data averaging. We consider these values to be our practical temperature sensitivity because they combine the TCR of the sensors and the measurement noise. This indicates that there is a trade-off between measurement speed and sensitivity because averaging will make the measurement overall slower but reduces the noise. The achieved sensitivity is already sufficient for some biomedical applications like skin[42] or breast[43] cancer detection, which require a sensitivity of ~0.5-2.2 °C, and wound healing[44] where infections would also show temperature differences of the order ~1.5 °C. However, for some applications a higher sensitivity may be needed. The sensors used here have a high resistance ~MΩ due to the low doping concentration in MoS_2. Increasing doping, e.g., through electrostatic gating, will reduce resistance but also lower the (absolute) TCR.[7] Thus, we expect that an optimum range with highest sensitivity can be found in the future.

Supporting references

1. Daus, A.; Vaziri, S.; Chen, V.; Köroğlu, Ç.; Grady, R. W.; Bailey, C. S.; Lee, H. R.; Schauble, K.; Brenner, K.; Pop, E., High-performance flexible nanoscale transistors based on transition metal dichalcogenides. *Nature Electronics* **2021,** *4*, 495-501.
2. Smithe, K. K.; Suryavanshi, S. V.; Muñoz Rojo, M.; Tedjarati, A. D.; Pop, E., Low variability in synthetic monolayer MoS_2 devices. *ACS Nano* **2017,** *11* (8), 8456-8463.
3. Smithe, K. K.; English, C. D.; Suryavanshi, S. V.; Pop, E., Intrinsic electrical transport and performance projections of synthetic monolayer MoS_2 devices. *2D Materials* **2017,** *4* (1), 011009.
4. Nassiri Nazif, K.; Daus, A.; Hong, J.; Lee, N.; Vaziri, S.; Kumar, A.; Nitta, F.; Chen, M. E.; Kananian, S.; Islam, R.; Kim, K.-H.; Park, J.-H.; Poon, A. S. Y.; Brongersma, M. L.; Pop, E.; Saraswat, K. C., High-specific-power flexible transition metal dichalcogenide solar cells. *Nature Communications* **2021,** *12*, 7034.
5. Zhu, W.; Low, T.; Lee, Y.-H.; Wang, H.; Farmer, D. B.; Kong, J.; Xia, F.; Avouris, P., Electronic transport and device prospects of monolayer molybdenum disulphide grown by chemical vapour deposition. *Nature Communications* **2014,** *5*, 3087.
6. Yu, Z.; Pan, Y.; Shen, Y.; Wang, Z.; Ong, Z.-Y.; Xu, T.; Xin, R.; Pan, L.; Wang, B.; Sun, L.; Wang, J.; Zhang, G.; Zhang, Y. W.; Shi, Y.; Wang, X., Towards intrinsic charge transport in monolayer molybdenum disulfide by defect and interface engineering. *Nature Communications* **2014,** *5*, 5290.
7. Khan, A. I.; Khakbaz, P.; Brenner, K. A.; Smithe, K. K.; Mleczko, M. J.; Esseni, D.; Pop, E., Large temperature coefficient of resistance in atomically thin two-dimensional semiconductors. *Applied Physics Letters* **2020,** *116* (20), 203105.
8. Kumar, A.; Schauble, K.; Neilson, K. M.; Tang, A.; Ramesh, P.; Wong, H.-S. P.; Pop, E.; Saraswat, K. In *Sub-200 Ω·μm alloyed contacts to synthetic monolayer MoS_2*, IEEE International Electron Devices Meeting (IEDM), IEEE: 2021; pp 7.3.1-7.3.4.
9. Röhr, J. A.; MacKenzie, R. C., Analytical description of mixed ohmic and space-charge-limited conduction in single-carrier devices. *Journal of Applied Physics* **2020,** *128* (16), 165701.
10. Dacuña, J.; Salleo, A., Modeling space-charge-limited currents in organic semiconductors: Extracting trap density and mobility. *Physical Review B* **2011,** *84* (19), 195209.
11. Rose, A., Space-charge-limited currents in solids. *Physical Review* **1955,** *97* (6), 1538.
12. Schricker, A. D.; Davidson III, F. M.; Wiacek, R. J.; Korgel, B. A., Space charge limited currents and trap concentrations in GaAs nanowires. *Nanotechnology* **2006,** *17* (10), 2681.
13. Cui, X.; Shih, E.-M.; Jauregui, L. A.; Chae, S. H.; Kim, Y. D.; Li, B.; Seo, D.; Pistunova, K.; Yin, J.; Park, J.-H.; Choi, H.-J.; Lee, Y. H.; Watanabe, K.; Taniguchi, T.; Kim, P.; Dean, C. R.; Hone, J. C., Low-temperature ohmic contact to monolayer MoS_2 by van der Waals bonded Co/h-BN electrodes. *Nano Letters* **2017,** *17* (8), 4781-4786.
14. Oversluizen, G.; Nieuwesteeg, K.; Boogaard, J., Meyer–Neldel rule in the space-charge-limited conduction of hydrogenated amorphous silicon. *Applied Physics Letters* **1991,** *59* (3), 312-314.
15. Schauer, F.; Zmeškal, O., Temperature dependent SCLC in amorphous silicon. *Journal of Non-Crystalline Solids* **1993,** *164*, 537-540.
16. Salvatore, G. A.; Sülzle, J.; Dalla Valle, F.; Cantarella, G.; Robotti, F.; Jokic, P.; Knobelspies, S.; Daus, A.; Büthe, L.; Petti, L.; Kirchgessner, N.; Hopf, R.; Magno, M.;

Tröster, G., Biodegradable and highly deformable temperature sensors for the internet of things. *Advanced Functional Materials* **2017,** *27* (35), 1702390.
17. Webb, R. C.; Bonifas, A. P.; Behnaz, A.; Zhang, Y.; Yu, K. J.; Cheng, H.; Shi, M.; Bian, Z.; Liu, Z.; Kim, Y.-S.; Yeo, W.-H.; Park, J. S.; Song, J.; Li, Y.; Huang, Y.; Gorbach, A. M.; Rogers, J. A., Ultrathin conformal devices for precise and continuous thermal characterization of human skin. *Nature Materials* **2013,** *12* (10), 938-944.
18. Mandal, S.; Banerjee, M.; Roy, S.; Mandal, A.; Ghosh, A.; Satpati, B.; Goswami, D. K., Organic field-effect transistor-based ultrafast, flexible, physiological-temperature sensors with hexagonal barium titanate nanocrystals in amorphous matrix as sensing material. *ACS Applied Materials & Interfaces* **2018,** *11* (4), 4193-4202.
19. Shin, J.; Jeong, B.; Kim, J.; Nam, V. B.; Yoon, Y.; Jung, J.; Hong, S.; Lee, H.; Eom, H.; Yeo, J.; Choi, J.; Lee, D.; Ko, S. H., Sensitive wearable temperature sensor with seamless monolithic integration. *Advanced Materials* **2020,** *32* (2), 1905527.
20. Yang, J.; Wei, D.; Tang, L.; Song, X.; Luo, W.; Chu, J.; Gao, T.; Shi, H.; Du, C., Wearable temperature sensor based on graphene nanowalls. *RSC Advances* **2015,** *5* (32), 25609-25615.
21. Wang, C.; Xia, K.; Zhang, M.; Jian, M.; Zhang, Y., An all-silk-derived dual-mode e-skin for simultaneous temperature–pressure detection. *ACS Applied Materials & Interfaces* **2017,** *9* (45), 39484-39492.
22. Harada, S.; Kanao, K.; Yamamoto, Y.; Arie, T.; Akita, S.; Takei, K., Fully printed flexible fingerprint-like three-axis tactile and slip force and temperature sensors for artificial skin. *ACS Nano* **2014,** *8* (12), 12851-12857.
23. Liu, G.; Tan, Q.; Kou, H.; Zhang, L.; Wang, J.; Lv, W.; Dong, H.; Xiong, J., A flexible temperature sensor based on reduced graphene oxide for robot skin used in internet of things. *Sensors* **2018,** *18* (5), 1400.
24. Oh, J. H.; Hong, S. Y.; Park, H.; Jin, S. W.; Jeong, Y. R.; Oh, S. Y.; Yun, J.; Lee, H.; Kim, J. W.; Ha, J. S., Fabrication of high-sensitivity skin-attachable temperature sensors with bioinspired microstructured adhesive. *ACS Applied Materials & Interfaces* **2018,** *10* (8), 7263-7270.
25. Liao, F.; Lu, C.; Yao, G.; Yan, Z.; Gao, M.; Pan, T.; Zhang, Y.; Feng, X.; Lin, Y., Ultrasensitive flexible temperature-mechanical dual-parameter sensor based on vanadium dioxide films. *IEEE Electron Device Letters* **2017,** *38* (8), 1128-1131.
26. Gong, X.; Zhang, L.; Huang, Y.; Wang, S.; Pan, G.; Li, L., Directly writing flexible temperature sensor with graphene nanoribbons for disposable healthcare devices. *RSC Advances* **2020,** *10* (37), 22222-22229.
27. Kuzubasoglu, B. A.; Sayar, E.; Cochrane, C.; Koncar, V.; Bahadir, S. K., Wearable temperature sensor for human body temperature detection. *Journal of Materials Science: Materials in Electronics* **2021,** *32* (4), 4784-4797.
28. Moser, Y.; Gijs, M. A., Miniaturized flexible temperature sensor. *Journal of Microelectromechanical Systems* **2007,** *16* (6), 1349-1354.
29. Wang, Y.-F.; Sekine, T.; Takeda, Y.; Yokosawa, K.; Matsui, H.; Kumaki, D.; Shiba, T.; Nishikawa, T.; Tokito, S., Fully printed PEDOT: PSS-based temperature sensor with high humidity stability for wireless healthcare monitoring. *Scientific Reports* **2020,** *10*, 2467.
30. Tian, M.; Huang, Y.; Wang, W.; Li, R.; Liu, P.; Liu, C.; Zhang, Y., Temperature-dependent electrical properties of graphene nanoplatelets film dropped on flexible substrates. *Journal of Materials Research* **2014,** *29* (11), 1288-1294.

31. Mahmoud, W. E.; Al-Bluwi, S. A., Development of highly sensitive temperature sensor made of graphene monolayers doped P(VDF-TrFE) nanocomposites. *Sensors and Actuators A: Physical* **2020,** *312*, 112101.
32. Hilal, M.; Han, J. I., Development of a highly flexible and durable fiber-shaped temperature sensor based on graphene/Ni double-decked layer for wearable devices. *IEEE Sensors Journal* **2020,** *20* (10), 5146-5154.
33. Liu, Q.; Tai, H.; Yuan, Z.; Zhou, Y.; Su, Y.; Jiang, Y., A high-performances flexible temperature sensor composed of polyethyleneimine/reduced graphene oxide bilayer for real-time monitoring. *Advanced Materials Technologies* **2019,** *4* (3), 1800594.
34. Wu, J.; Huang, W.; Liang, Y.; Wu, Z.; Zhong, B.; Zhou, Z.; Ye, J.; Tao, K.; Zhou, Y.; Xie, X., Self-calibrated, sensitive, and flexible temperature sensor based on 3D chemically modified graphene hydrogel. *Advanced Electronic Materials* **2021,** *7* (4), 2001084.
35. Ozioko, O.; Kumaresan, Y.; Dahiya, R. In *Carbon nanotube/PEDOT:PSS composite-based flexible temperature sensor with enhanced response and recovery time*, 2020 IEEE International Conference on Flexible and Printable Sensors and Systems (FLEPS), IEEE: 2020; pp 1-4.
36. Chen, Z.; Zhao, D.; Ma, R.; Zhang, X.; Rao, J.; Yin, Y.; Wang, X.; Yi, F., Flexible temperature sensors based on carbon nanomaterials. *Journal of Materials Chemistry B* **2021,** *9* (8), 1941-1964.
37. Wu, Z.; Li, C.; Hartings, J.; Ghosh, S.; Narayan, R.; Ahn, C., Polysilicon-based flexible temperature sensor for brain monitoring with high spatial resolution. *Journal of Micromechanics and Microengineering* **2016,** *27* (2), 025001.
38. Lugoda, P.; Costa, J. C.; Oliveira, C.; Garcia-Garcia, L. A.; Wickramasinghe, S. D.; Pouryazdan, A.; Roggen, D.; Dias, T.; Münzenrieder, N., Flexible temperature sensor integration into e-textiles using different industrial yarn fabrication processes. *Sensors* **2020,** *20* (1), 73.
39. Xiao, Y.; Jiang, S.; Li, Y.; Zhang, W., Screen-printed flexible negative temperature coefficient temperature sensor based on polyvinyl chloride/carbon black composites. *Smart Materials and Structures* **2021,** *30* (2), 025035.
40. Liao, F.; Zhu, Z.; Yan, Z.; Yao, G.; Huang, Z.; Gao, M.; Pan, T.; Zhang, Y.; Li, Q.; Feng, X.; Lin, Y., Ultrafast response flexible breath sensor based on vanadium dioxide. *Journal of Breath Research* **2017,** *11* (3), 036002.
41. Park, J.; Kim, M.; Lee, Y.; Lee, H. S.; Ko, H., Fingertip skin–inspired microstructured ferroelectric skins discriminate static/dynamic pressure and temperature stimuli. *Science Advances* **2015,** *1* (9), e1500661.
42. Çetingül, M. P.; Herman, C., Quantification of the thermal signature of a melanoma lesion. *International Journal of Thermal Sciences* **2011,** *50* (4), 421-431.
43. Zhou, Y.; Herman, C., Optimization of skin cooling by computational modeling for early thermographic detection of breast cancer. *International Journal of Heat and Mass Transfer* **2018,** *126*, 864-876.
44. Fierheller, M.; Sibbald, R. G., A clinical investigation into the relationship between increased periwound skin temperature and local wound infection in patients with chronic leg ulcers. *Advances in Skin & Wound Care* **2010,** *23* (8), 369-379.